

Direct observation of photonic spin Hall effect in Mie scattering

Aizaz Khan^{1,2,†}, Nikolay Solodovchenko^{3,†}, Dongliang Gao^{1,*}, Denis Kislov⁴, Xiaoying Gu¹, Yuchen Sun⁵, Lei Gao^{1,2,*},
Cheng-Wei Qiu^{6*}, Alexey Arsenin⁴, Alexey Bolshakov⁴, Vjaceslavs Bobrovs⁷, Alexander S. Shalin^{2,4,8,9*}

¹ School of Physical Science and Technology, Soochow University, Suzhou 215006, China & Jiangsu Key Laboratory of Frontier Material Physics and Devices, Soochow University, Suzhou 215006, China.

² School of Optical and Electronic Information, Suzhou City University & Suzhou Key Laboratory of Biophotonics & Jiangsu Key Laboratory of Biophotonics, Suzhou 215104, China.

³ School of Physics and Engineering, ITMO University, Saint-Petersburg 197101, Russia.

⁴ Moscow Center for Advanced Studies, Kulakova str. 20, Moscow 123592, Russia.

⁵ School of Electrical and Electronic Engineering, 50 Nanyang Avenue, Nanyang Technological University, Singapore, 639798, Singapore.

⁶ Department of Electrical and Computer Engineering, National University of Singapore, Singapore 117583, Singapore.

⁷ Riga Technical University, Institute of Photonics, Electronics and Telecommunications, 1048 Riga, Latvia

⁸ Centre for Photonic Science and Engineering, Skolkovo Institute of Science and Technology, Moscow, 121125, Russia.

⁹ Beijing Institute of Technology Beijing 100081, China

Emails: DL Gao: dlgao@suda.edu.cn; L Gao: leigao@suda.edu.cn; C-W Qiu: chengwei.qiu@nus.edu.sg;

A Shalin: alexandesh@gmail.com

Abstract:

The photonic spin Hall effect, a hallmark of spin-orbit interaction in light, has emerged as a platform for spin-dependent applications in nanophotonics. Due to intrinsic weak spin-orbit interaction, the resultant shift is tiny with drastically low scattering efficiency, which necessitates signal amplification and high-precision weak measurements for detection - often at the cost of further lowering the intensity. This dilemma between the photonic spin Hall shift and the scattered intensity becomes even more pronounced when the geometry shrinks to the scale of a single particle. Owing to the inherent inverse relation between the spin Hall shift and the scattering intensity, the shift is typically enhanced as a result of destructive interference in Kerker scattering, accompanied by a significant suppression of the scattering intensity. This trade-off poses a fundamental challenge for the direct far-field observation of the photonic spin Hall shift from a standalone nanoparticle. Here, we overcome this dilemma by breaking the rotational symmetry of the scatterer to induce multipolar coupling along with strong spin-orbit coupling, resulting in superscattering that boosts the scattering intensity at the maximal photonic

spin Hall shift by two orders of magnitude compared to conventional dipolar particle. By tailoring the multipolar interference, the photonic spin Hall shift is enhanced at an angle feasible for direct observation. In doing so, we perform a post-selection-free experiment to bypass the loss in intensity and preserve both the spin Hall shift and the scattering efficiency. We have, for the first time, experimentally demonstrated the predicted photonic spin Hall shift for a standalone particle through measurable differences in far-field scattering intensity in the microwave regime. These findings pave the way for a deeper exploration of the spin Hall effect of light and open new avenues for applications in precision metrology and advanced optical imaging.

Introduction: The spin Hall effect is probably one of the most striking effects in electronic or photonic systems. The effect originates from the spin-orbit interaction (SOI) of electrons or photons. Akin to the spin Hall effect in electronic systems¹, the photonic spin Hall shift (PSHS) refers to a transverse beam shift of the reflected, refracted or scattered light^{2,3}. Scattering from high-index dielectric particles substituted plasmonic structures and provided a control over the spatial and temporal of light, which has opened a new field of resonant meta-photonics known as Mie-tronics^{4, 5, 6}. While the shift of photons has been predicted and explained in theory for more than 90 years⁷, direct observation of PSHS in scattering is still challenging because the SOI of light is usually very weak. For the PSHS at a planar interface, quantum weak measurements^{8,9} or multiple reflections^{10,11} are exploited to amplify and detect tiny shifts in experiments, which arises intrinsically by lowering the reflectivity/refractivity of the incident polarized state, which plummet the intensity and so leads to the enhanced but inefficient PSHS, in exception to few^{12,13}. Hence, to observe the spin-dependent shift, enhanced PSHS with high efficiency is most desired, which can be realized by using metamaterial and metasurface^{13, 14, 15}. Recently, an all-dielectric metasurface has been proposed to simultaneously enhance the shift and efficiency of PSHS in the optical regime¹².

As the geometry scales down to the level of single nanoparticle, in addition to weak spin-orbit

coupling, the intrinsic dilemma between the PSHS and intensity becomes adverse and presents a significant obstacle to direct observation of PSHS in the experiment even at the normal incidence. For example, the PSHS from spherical nanoparticles can be greatly enhanced in dual symmetric systems¹⁶,¹⁷. However, owing to the inverse relationship between the PSHS and the scattering intensity, the enhancement of PSHS arises at wavelengths attributed to Kerker conditions¹⁸, where destructive interference suppresses scattering intensity to nearly zero at the precise angles corresponding to maximum PSHS. As illustrated in Fig. 1, signal amplification through post-selection inherently comes at the cost of further reducing intensity, making it extremely challenging to apply in measuring such subtle optical localization errors in the position of a standalone scatterer. Thereafter, the direct observation of PSHS from standalone particle elevates the need for simultaneous enhancement of near-field SOI and far-field scattering efficiency. For example, a theoretical approach based on morphology optimization that leads to efficient PSHS was realized by overlapping the electric and magnetic modes at their resonance¹⁹ rather than their tails. Despite a nearly one-order enhancement in scattering intensity, the intensity remains intrinsically weak, and its detection is further hindered by experimental constraints—most notably, the positioning of the excitation antenna, which obstructs the scattered light and presents a shadowing effect for the detecting waveguide at the large angles where the PSHS reaches its maximum.

Here, we show that superscattering in subwavelength 3D systems²⁰ can greatly boost the efficiency of far-field scattering, when the SOI in the near-field is enhanced as well. Compared to the intuitive method that increases the scattering intensity by overlapping the electric and magnetic modes at their resonance, here, the modes interference mechanism (governing bound states in the continuum in standalone particles) pushes multipoles and the overall scattering cross-section (SCS) above the single-channel limit^{21, 22}. By breaking the spherical symmetry, power exchange becomes possible between multipole resonances, which results in super-dipolar modes from a spheroid nanoparticle. The scattering intensity is increased by almost two orders at the angles of enhanced PSHS. Moreover, the

slope of the azimuthal component of the Poynting vector turns positive, leading to pronounced helical flow and hence the scattering angles of the maximum shift (around 124°) are not close to the backward direction, as that (around 160°) in conventional dual systems¹⁶, which facilitates the direct observation of PSHS. Our first-to-date post-selection free microwave experiment shows that the detected shifts and scattering intensity agree well with the predicted ones by theory.

Results:

We start our analysis by overviewing the problem of low intensity $i(\theta)$ in conventional cases for enhanced PSHS. When an incident light in the pure state is scattered from a particle, the spiralling power flow results in a shift of the perceived location of the particle. This so-called PSHS is perpendicular to the scattering plane. For a finite-size particle, the magnitude of the shift can be obtained in the far-field by the pure geometric argument, beyond the dipolar regimes as^{23, 24},

$$\Delta_{SH} = \lim_{r \rightarrow \infty} r(-S_\phi / S_r)\hat{\phi}, \quad (1)$$

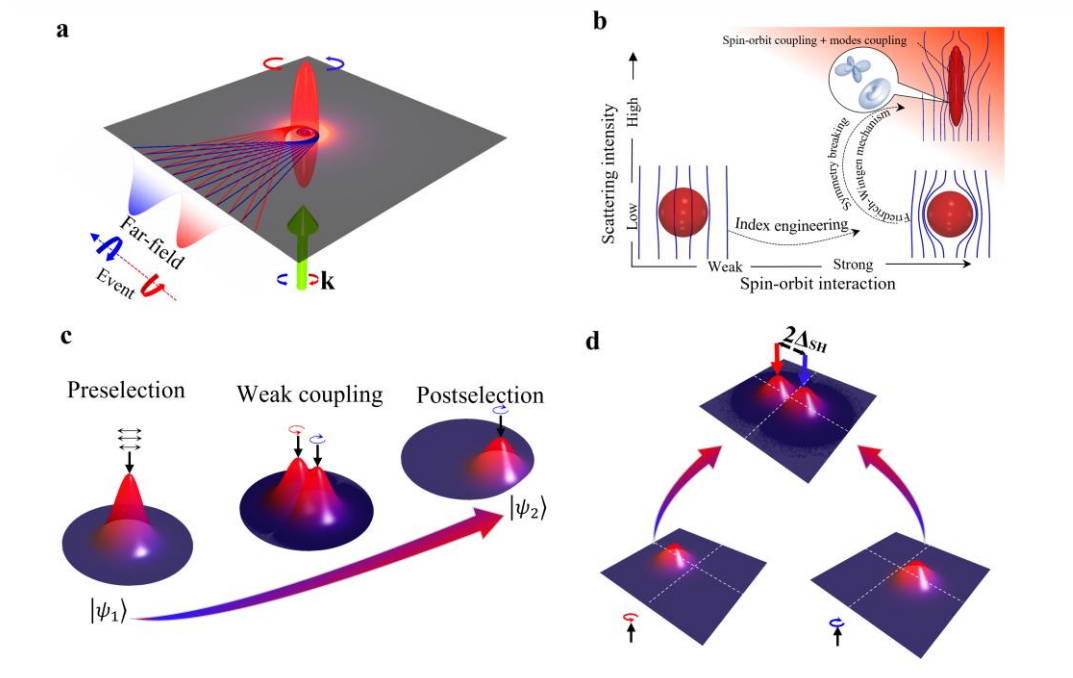


Fig. 1| Artistic view of simultaneous spin-orbit and modes coupling induce post-selection free observation of spin Hall effect: **a** Schematics of helicity dependent vortices arise due to strong spin-orbit coupling exhibited by the scattered Poynting vector upon excitation of light in pure state of polarization at distinct events. The rotation of vortex depends on the incident helicity due to which the scattered intensity at a particular observation

direction in the far-field is shifted in each event by an equal amount in opposite direction. The difference between the maxima is always twice the shift in the position. **b** Illustration of the trade-off between the near-field spin-orbit interaction (photonic spin-Hall shift) and the far-field scattering intensity. The weak spin-orbit interaction in low-index particles is brought to the regime of strong coupling through index engineering i.e., by replacing the particle with high index spherical particle. The strong SOI is exhibited in the near-field at incident wavelengths attributed to the Kerker conditions, with sufficiently low intensity. By breaking the rotational symmetry, modes' coupling is induced together with the strong spin-orbit coupling, which simultaneously results in enhanced spin-Hall shift and scattering intensity. For direct observation, our goal is to achieve both strong coupling of spin and orbital angular momentum via rapid optical potential-gradient and high scattering intensity through superscattering induced by Friedrich-Wintgen mechanism (top right). **c** Artistic view of intensity loss during post-selection in conventional weak measurement. **d** Schematic of post-selection free reconstruction of the shift in the perceived location of an isolated particle along the transverse direction through the scattered intensity, sharing the same spatial region during different events with respect to the incident helicity.

where r is the radial distance, S_ϕ and S_r are the azimuthal and radial components of the Poynting vector \mathbf{S} , respectively. An intuitive approach to enhanced PSHS is to simultaneously excite the electric and magnetic modes exhibiting the same magnitude, which is theoretically realized in particles satisfying electromagnetic dual symmetry¹⁶. However, dual symmetry for spherical scatterers usually requires the first Kerker condition to be satisfied¹⁸, where the scattering coefficients of electric and magnetic modes should be exactly equal and in phase²⁵. On the other hand, the intensity $i(\theta)$ is proportional to the amplitude square of the scattering coefficients ([see supporting information](#)). Thus, it is preliminary for the PSHS to be enhanced simultaneously with high far-field intensity at angle of enhance PSHS if they interfere at their resonances rather than the tails. Morphology optimization of dual scatterers provides one route to achieve high intensity, while preserving the enhanced magnitude of PSHS¹⁹. However, there is a caveat rooted in the first Kerker condition: due to destructive interference, the PSHS tends to enhance in the backscattered direction with a resonance at the tail of the scattering angle θ , where the far-field intensity faces an inherent dilemma of plummeting to zero in the case of conventional targets¹⁹. Fundamentally, the complete destructive interference at these angles is tied with the negative or zero slope of the radial and azimuthal components of the Poynting

vector along the observation direction as Mie theory predicts in light scattered from conventional particles (see supporting information). A direct observation scheme thus pushes the scattering from a standalone particle to achieve high intensity and PSHS in the far-field at observation directions free from shadowing effects together with strong SOI in the near-field, all at the same time.

Superscattering on the other hand strengthen light-matter interaction by breaking the single-channel limit either by forming the super multipoles²¹ or overlapping several multipole resonances^{20, 26}, which is ideal to enhance the scattering intensity. Without the loss of generality, we process with left circularly polarized light (LCP) defined as a superposition of x and y -polarized light propagating in the z -direction, i.e., $\mathbf{E}^{inc} = e^{ikz}(\hat{x} - i\hat{y})$, impinges on high-index particle (to induce strong SOI) with otherwise broken rotational symmetry. To obtain the SCS, intensity as well as the PSHS, the scattered electric \mathbf{E}^{sca} and magnetic \mathbf{H}^{sca} fields are expanded into the series summation form of the spheroidal vector wave function $\mathbf{M}_{omn}^{(3)}$ and $\mathbf{N}_{omn}^{(3)}$ ²⁷.

$$\mathbf{E}^{sca} = \sum_{n=1}^{\infty} i^n \left(i\alpha_n \mathbf{N}_{emn}^{(3)} - \beta_n \mathbf{M}_{omn}^{(3)} + \alpha_n \mathbf{N}_{omn}^{(3)} - i\beta_n \mathbf{M}_{emn}^{(3)} \right), \quad (2)$$

$$\mathbf{H}^{sca} = \frac{k}{i\omega\mu} \sum_{n=1}^{\infty} i^n \left(i\alpha_n \mathbf{M}_{e1n}^{(3)} - \beta_n \mathbf{N}_{o1n}^{(3)} + \alpha_n \mathbf{M}_{o1n}^{(3)} - i\beta_n \mathbf{N}_{e1n}^{(3)} \right), \quad (3)$$

where, the coefficients of the incident, scattered and internal fields can be obtained by solving the boundary conditions²⁷. As the incident field propagates normally along the z -axis, the subscript m can be taken as unity, whereas the o and e represent odd and even dependence corresponding to $\sin(m\phi)$ and $\cos(m\phi)$. Note that the expressions and calculations are all in spheroidal coordinate system, one can easily transform the fields into spherical coordinates.

At this stage, by using scattered and incident fields, we obtained the total SCS which is defined as $\sigma = \lim_{r \rightarrow \infty} 4\pi r^2 |\mathbf{E}^{sca}|^2 / |\mathbf{E}^{inc}|^2$ (see supplementary information). To achieve superscattering, the total SCS must greatly surpass the SCS of a dipolar particle with spherical symmetry. The maximum contribution to SCS by each multipole is bound to $\sigma_{\max} = (2n+1)\lambda^2 / 2\pi$ for a standalone spherical

particle in free space, where n is the scattering channel, i.e., $n=1$ for a dipole, $n=2$ for a quadrupole and so on. This is the so called “single-channel limit”²⁶. Thus, arbitrarily large total SCS can be obtained by the conventional mechanism of superscattering by maximizing the contributions of sufficient number of channels (multipoles)²⁰. On the other hand, the broken spherical symmetry can induce mode coupling providing that a single or several multipoles receive contribution from other multipoles and resulting in the formation of super multipoles²¹. Thus, the total contribution from a single multipole to the SCS is no longer limited by the single-channel limit as explained by the Friedrich-Wintgen mechanism^{21, 28}. In the following we show that for some particles it is possible to enhanced scattering by both mechanisms of overlapping multipolar resonances and the super-multipoles.

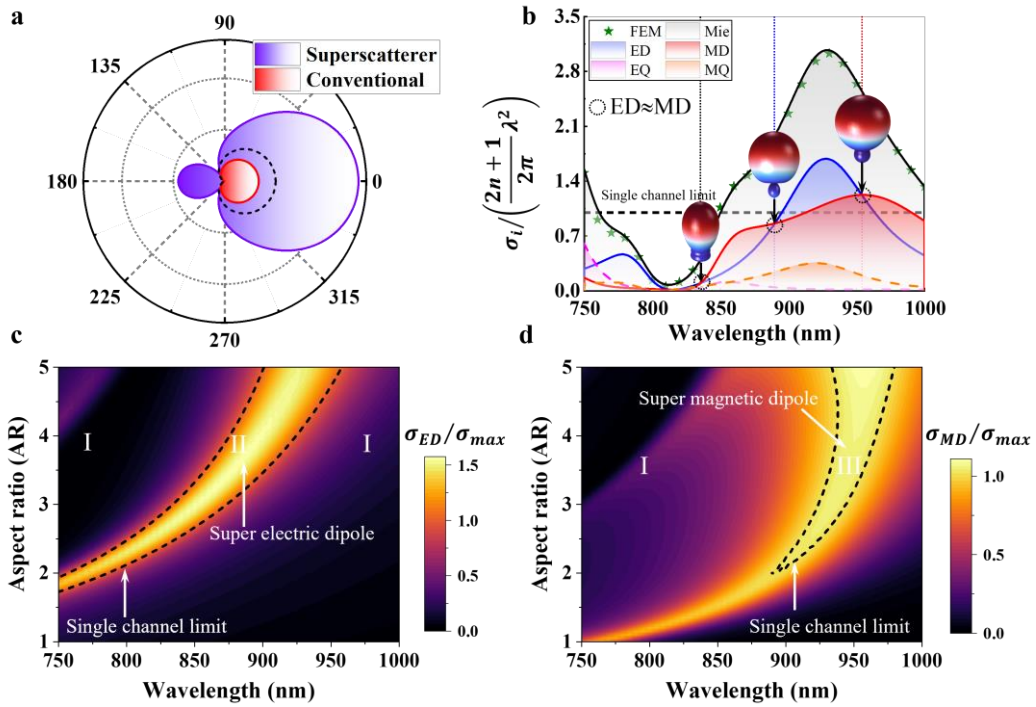


Fig. 2| Superscattering emerges from super electric and super magnetic dipoles: **a** The far-field radiation patterns suitable for enhancing PSHS. The red loop represents conventional scatterers at first Kerker conditions bounded by single channel limit (black dashed line). The blue loop represents superscatterer near the Kerker criteria with enhanced scattering far beyond the dipolar limits. **b** Partial contributions of constituent's multipoles as a function of incident wavelength. Super dipoles contribute to total scattering cross-section and drive superscattering (exceeding single-channel limit three times that of the single-channel limit). The far-field radiation patterns at various wavelengths corresponding to the overlapping electric and magnetic dipoles are

presented in the inset of **b**. The superscatterer is defined by its aspect ratio (AR, defined as a/b), with a been the semi-major axis (500 nm) that is aligned in the incident direction of the wave, and the semi-minor axis b (100 nm). **c**, **d** The smooth deformation of a sphere (radius = 100 nm) to a prolate spheroid induces mode coupling and gives rise to **c** super electric (region II) and **d** super magnetic (region III) dipoles that surpass the fundamental dipolar limit (black dashed line) in a broad spectral region. In region I, both electric and magnetic dipoles are lower than the single channel limit. The refractive index of the particle is taken as that of silicon and the particle is embedded in air.

To establish a consistent comparison of scattering enhancement, we normalized the scattering cross-section of each multipole by the corresponding maxima defined by $\sigma_{\max} = (2n+1)\lambda^2 / 2\pi$. If σ_i is the scattering cross-section due to a single-channel, then the quantity σ_i / σ_{\max} is usually less than 1 for a conventional scatterer, with a maximum possible value that can be achieved under the condition $\sigma_i = \sigma_{\max}$ is 1. In what follows, super electric and super magnetic dipoles emerge by breaking the rotational symmetry of the sphere in the direction parallel to the propagation direction to form a prolate spheroid, as illustrated in Fig. 2b. The contribution from super electric and super magnetic dipoles greatly enhances scattering and pushes the total SCS beyond the single channel limit, as shown in Fig. 2b. By maintaining a constant equatorial radius and changing the polar radius of the prolate spheroid through the variations in aspect ratio, both super electric and super magnetic dipoles emerge around $AR \sim 1.5$, whereas both the super electric and super magnetic dipoles vanishes as the AR approaches unity (sphere), as illustrated in Fig. 2c,d. This amplification of the total SCS is primarily due to the enhanced contribution from the super multipoles in that wavelength range. Therefore, by breaking the spherical symmetry, we have achieved superscattering in a standalone 3D scatterer via super multipoles and the accidental overlap. By being able to enhance the contribution of dipolar channels and interfering them near their resonances in the superscattering regime, one can enhance light-matter interaction to bring the intensity at the peak PSHS with strong spin-orbit coupling, to a detectible level in stark contrast with conventional dual particles^{16, 17, 19}, as demonstrated in Fig. 2a. In the following, we show that such superscatterer drastically boosts the intensity at the observation angle which is suitable for an experimental observation of the enhanced PSHS.

In near-field, strong SOI results the far-field PSHS, which merely depends upon the scattering angle θ , provided that the scatterer is a dipole²⁹. However, for a finite-sized particle, the PSHS depends on both the optical properties of particle and the scattering angle. Therefore, the enhanced PSHS arises at a certain scattering angle θ accompanied by strong SOI, which is mediated by the large discrepancy of the optical constant at air-particle interface, resulting in large optical potential gradient²³. Generally, the mutual relation between the PSHS and the far-field intensity is inverse, with a similar analogy in 2D cases. At the level of single particle, the intensity is tied to the radial component of the Poynting vector S_r . Meanwhile, the PSHS is enhanced if the radial component S_r is small as a direct consequence of Eq. 1. A parallel comparison can be made in planar interfaces, where the reflectivity of incident polarization is greatly suppressed while enhancing that of other polarization to achieve enhance PSHS³⁰. Thus, to directly observe PSHS in the case of scattering from standalone particle, the azimuthal component must be relatively enhanced in contrast to completely suppressing the radial component of the Poynting vector.

In Fig. 3, we state the challenge in experimental detection of the enhanced PSHS at the backscattered direction for conventional cases. First the scattered intensity is detected in a plane that is tangent to an imaginary sphere with radius r . At a fixed observation direction, the coordinates of this plane are defined by the dimensionless parameters $\mu = kx$ (transverse) and $\eta = ky$ (longitudinal). The continuous variation in the observation direction will lead to instantaneous tangent planes that eventually lie on the surface of the imaginary sphere enclosing the scatterer at its centre, as shown in Fig. 3a. For a conventional quasi-dual particle with spherical symmetry, the PSHS is enhanced by enforcing high directional scattering via satisfying the first Kerker conditions^{16, 17}. Thus, in the backscattered direction the destructive interference between electric and magnetic dipoles results in enhanced PSHS at the scattered angle around 160° . However, due to the overlapping dipoles at their tails, the far-field intensity is vanishingly small (red-panel in Fig. 3b) and is not enough to directly detect the enhance PSHS. Geometry optimization of conventional scatterers enforces the overlap of

scattering coefficients at their resonances, leading to enhanced intensity by one order (blue-panel)¹⁹. Yet, with low azimuthal and radial components of the Poynting vector, the resonance of PSHS lies at the extreme backscattered direction and is not suitable for direct experimental observation, as marked by conventional II in Fig. 3b.

To realize simultaneous enhance PSHS and its far-field efficiency, a superscatterer at incident wavelength 890 nm (blue-dotted line in Fig. 2b) is exploited. When the particle is in the superscattering condition, the enhancement of the PSHS is observed at a scattering angle $\sim 124^\circ$, as shown by the black line in Fig. 3b. At the same time, the far-field intensity at the maximal PSHS is enhanced by 100 times that of the conventional spherical particle, as shown in Fig. 3b. In addition to large radial component of the Poynting vector, the morphology of superscatterer induces a helical flow around the particle, leading to a large azimuthal component as well in stark contrast to conventional scatterers¹⁶ ([see supporting information](#)). This empowers both PSHS and the associated intensity at the scattering angle suitable for direct observation. It is to be noted that unlike earlier works of PSHS, we have assumed tiny losses in the particle as all the results in our work consider a realistic particle rather than only fixed permittivity with no loss. In stark contrast to conventional particles, both the enhanced far-field PSHS and the intensity are obtained for superscatterer, and the angle of maximal PSHS is much smaller and suitable for experimental observation. With preserved enhanced PSHS, the intensity is almost 100 times that of for conventional dipolar particle at maximal PSHS. These are the main hallmarks of the current work, which allow experimental feasibility for direct observation of enhanced far-field PSHS.

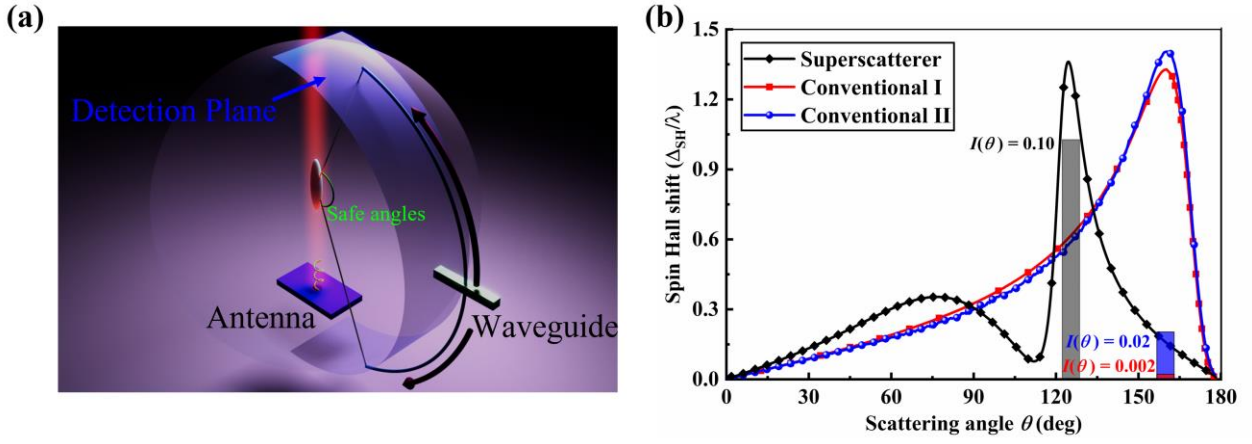


Fig. 3| Superscattering driven simultaneous enhancement of photonic spin Hall shift and scattering intensity: **a** Artistic representation of the experimental setup representing the limitations of large angle detection.. In the detection plane, the scattered field is blocked from the detector (waveguide) by the antenna in the backscattered direction, which poses a challenge in detection of enhanced photonic spin Hall shift (PSHS) in conventional cases. **b** The far-field photonic spin Hall shift and far-field intensity for the considered particle in the superscattering regime and conventional scatterers. The far-field intensity for the superscatterer (black-panel) drastically surpasses those for the conventional scatterers (red and blue-panel) at the maximal PSHS. For numerical calculations, the refractive index for all three cases is taken as that of silicon, and the incident wavelength is chosen 890 nm. The optimal size for the conventional cases to achieve the same magnitude of PSHS at this wavelength is a diameter of 219 nm for conventional I and semi-major axis $a = 169$ nm with an aspect ratio of 0.5 for the conventional II. The superscatterer is defined by the same parameters as those of Fig. 2b. The peak PSHS lies at the tail of the backscattered direction for conventional scatterers, while for the superscatterer, the maximum PSHS appears at the scattered angle of $\theta \approx 124^\circ$. The incident polarization is taken as LCP.

The enhancement of PSHS in the far-field is fundamentally governed by the strength of SOI in the near-field^{31, 32}. Together with strong near-field SOI, the interference between the electric and magnetic multipolar modes affects the magnitude of the PSHS¹⁶. To demonstrate the SOI, we analysed the orbital momentum density as streamlines and characterized the polarization behaviour through the circular polarization degree (CPD) which is defined as $CPD = |\epsilon_0 \mathbf{E}^* \times \mathbf{E} + \mu_0 \mathbf{H}^* \times \mathbf{H}| / (\epsilon_0 |\mathbf{E}|^2 + \mu_0 |\mathbf{H}|^2)$ ³³. A field in pure state (circular-polarization) is characterized by $CPD = 1$, on the other hand, $CPD = 0$ is associated with linear polarization. In Fig. 4, we show the orbital momentum density streamlines and CPD for the cases where the electric and magnetic dipoles overlap (vertical dotted-lines in Fig. 2b).

The stark contrast of optical constants at the surface of the particle leads to rapidly changing optical potential and mediates strong SOI³³. Due to this the trajectory of photons in the near-field featuring singularities is strongly twisted, which is attributed to the low CPD in the near-field. Intriguingly, in Fig. 4b, the streamlines are significantly coiled as they reached the maximum geometric cross-section of the particle, while converge at the vortex singularity at the front of the particle. This spin flow arises at the incident wavelength of 890 nm (blue-dotted line in Fig. 2b), where the of super electric dipole and magnetic dipole interfere constructively in the forward direction. Contrary to this, overlapping electric and magnetic dipoles in superscattering region (red-dotted line in Fig. 2b) and a wavelength of non-superscattering region (black-dotted line in Fig. 2b) exhibits weak twisted stream lines and correspondingly low drop in CPD, as shown in Fig. 4a, c.

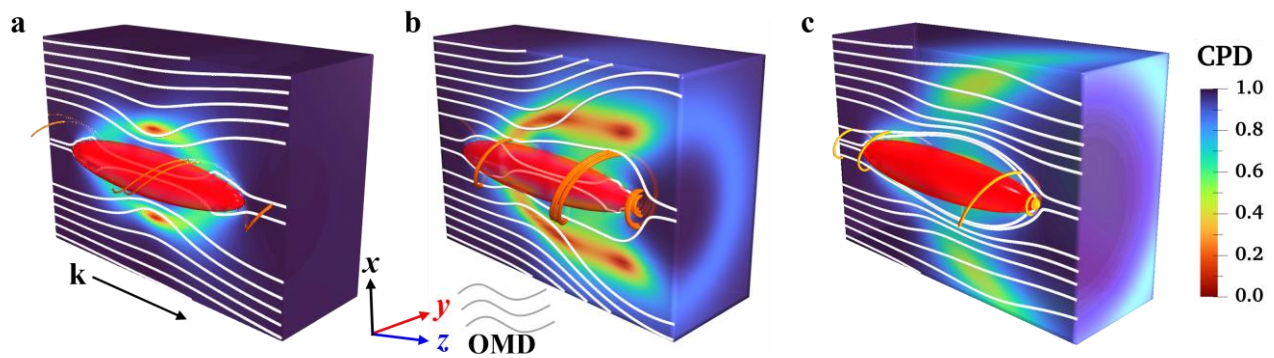


Fig. 4| Spin-orbit interaction in the near-field: The circular polarization degree (volume) of field and orbital momentum density as streamlines for the particle under equal electric and magnetic dipoles at various wavelengths falling within the **a** non-superscattering at wavelength 830 nm and **b, c** superscattering regimes at wavelengths 890 nm and 950 nm, as marked in Fig. 2b. The 3D volume represents the circular polarization degree in the near-field, with one-half across the plane passing through the center of the particle is shown and the other half is the exact replica of it. The red portions apart from the particle show regions where strong spin-orbit interaction arises and the polarization of the total field turns to linearly polarization due to complete spin flow. The streamlines in xz -plane are shown by the white lines, whereas they are shown in 3D by the orange colour. Saddle singularity guiding the photons in the forward direction can be seen xz -plane in front of the particle just after the vortex visualized in 3D. Strong coupling of orbital and spin angular momentum near the surface of the particle is mediated by the refractive index change, and the circular polarization degree drops significantly at the incident wavelength 890 nm. The parameters remained the same as in Fig. 2b except the polarization of the incident light is LCP.

It can be noted that the intensity will be far higher at the wavelength where the total SCS reaches its maximum and also at the overlapping dipoles (red-dotted line in Fig. 2b). However, the corresponding PSHS at this wavelength will be very small, primarily due to two reasons. As demonstrated in Fig. 4c, the trajectory of photons is weakly twisted with low fall in CPD, leading to comparatively low SOI in contrast to that of Fig. 4b. Secondly, the enhancement of PSHS is tied with overlapping multipoles in phase. While the super electric and magnetic dipoles do not overlap at the wavelength where total SCS reaches its peak, they are also not in phase at incident wavelength 950 nm. Thus, a suitable wavelength for both enhancement of PSHS and the intensity corresponds to the conditions where the multipoles overlap in phase along with strong SOI as that in Fig. 4b.

Experimental demonstration:

To verify our results, we performed a microwave experiment for a ceramic-based superscattering spheroid defined by semi-major axis $a = 25.995$ mm and semi-minor axis $b = 4.985$ mm, and optical parameters, permittivity $\epsilon' = 15.2$ and losses $\tan(\delta) \approx 10^{-4}$. Irrespective of the geometry of the underlying structure, the shift was usually determined experimentally by Stoke's parameters^{12, 34} or weak measurement⁸. Our experimental setup completely differs from the previous methods and closely resembles that of the proposed experimental setup in references^{19, 35}. In our setup, circularly polarized light is incident along the spheroidal axis. The exciting antenna is located at a distance of 50 cm, and is tuned to the frequency 6 GHz. The scattered field is detected in the far-field by a waveguide with a dipole inside, the operating frequency of which is in the range of 4.9 to 7 GHz. The distance from the spheroid to the dipole is about 120 cm. To register the scattered field only from the spheroid, it is necessary to detect the scattering matrix element S_{12} with and without the particle so that the difference in both measurements accounts for the removal of the background field and noise in the system. Since the rectangular waveguide detects only one polarization of the electric field along its short side, the

total scattered field was obtained by combining two mutually perpendicular components. To further reduce noise, the spectra for each component were averaged over 20 measurements. Since the particle rotates along with the emitting antenna while the receiving waveguide only moves up and down along the z -axis, the detector is almost always oriented towards the particle. Due to complex scattering, the detection of the original position of the particle in the scattering plane is challenging and so is the corresponding shift in the far-field. However, PSHS for RCP and LCP light have the same magnitude and opposite sign. It is then reasonable that the shift in the perceived location can be found from the difference of the maximum far-field intensity corresponding to different polarization at a particular scattering angle.

In what follows, we measure the far-field intensity for the excitation corresponding to light in the pure state of polarization (RCP and LCP) for various scattering angles in the vicinity of the peak of PSHS at the incident frequency 6.02 GHz. We determined the PSHS from the difference in the peak far-field intensity of the incident RCP and LCP waves. The results of experiment are in good agreement with theoretical and simulations, as shown in Fig. 5a. It should be noted that the difference in the peak intensities for RCP and LCP is always 2 times the shift in the perceived location. The experimental results must be reduced to half to get the PSHS. The far-field intensity for LCP is average over 20 measurements, and the resulting intensity is plotted along the scattering angle, which is in agreement with the theoretical prediction Fig. 5b. With $\varepsilon = \text{const}$, the experimentally obtained results can be generalized to the optical frequency range.

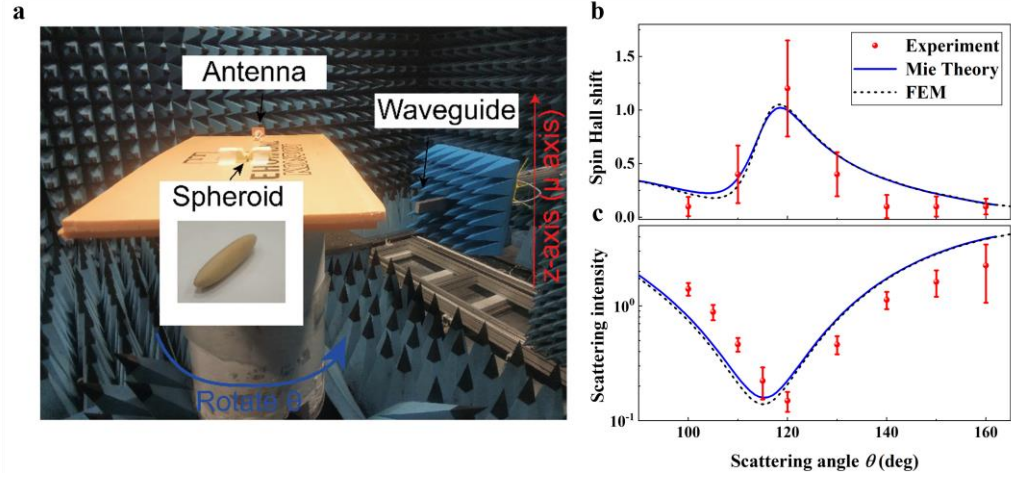


Fig. 5| Direct observation of the PSHS in the scattered field: a Far-field view of experimental setup, showing antenna, rectangular waveguide and the ceramic particle. The exciting frequency is 6.02 GHz, and the scatterer is made up of ceramic composite with semi-major axis $a = 25.995$ mm and semi-minor axis $b = 4.985$ mm. The permittivity of the scatterer for the theoretical curve is taken as $\epsilon' = 15.2$, losses $\tan(\delta) \approx 10^{-4}$. **b** Comparison of the experimental results for PSHS with the theoretical results obtained from Mie theory. **c** Experimentally obtained and theoretically calculated far-field intensity.

Discussions:

We demonstrate both theoretically and experimentally the simultaneous enhancement of the PSHS and the far-field scattering intensity by superscattering particle exhibiting strong near-field SOI. Our work marks the first-ever approach to direct experimental observation of the PSHS in scattered light. Previous works on the enhanced PSHS in dual scatterers entail low far-field intensity as a result of the first Kerker conditions, where the scattering intensity vanishes at the scattering angle of enhanced PSHS. Morphology optimization of dual scatterers can provide one route to achieve enhance intensity by the overlap of the scattering coefficients at their resonances rather than their tails. Yet, the enhancement in the case of the conventional scatterers lies at the tail of the backscattering angle near $\theta = 160^\circ$, which is hard to achieve experimentally, and so for the direct observation of PSHS remained challenging. Along with the first direct experimental observation of the PSHS, our work exhibits several merits. First, the simultaneous enhancement of the far-field PSHS and the far-field scattering intensity for a realistic particle with losses: the latter is one order higher than that of the optimized

conventional scatterers¹⁹ with the same PSHS, and that's why it becomes measurable. Secondly, the effect lies at the scattering angle, which does not lie in the extreme backward direction. Due to which we have directly observed the PSHS in scattering from single nanoparticle in experiment through a mechanism proposed in our early work¹⁹. Due to challenges in measuring the maximal PSHS at the extreme backscattered direction, no anticipated results were obtained there. Our approach is free from post-selection losses. Our breakthrough microwave experiment marks the first direct experimental observation of the PSHS, which can potentially enable new applications of PSHS at the scale of a single nanoparticle.

Methods:

Generalized Lorentz-Mie theory:

Scattering of electromagnetic waves from a spheroidal particle can be studied using the generalized Lorentz-Mie theory. Here we briefly introduce the main equations, the details of which can be found in the references^{27, 36}. For a homogenous particle defined by the spheroidal coordinates (η, ξ, φ) in an isotropic and homogenous medium illuminated by electromagnetic wave, the time-independent parts of the fields inside and outside the spheroid particle satisfy the vector wave equations²⁷.

$$\nabla^2 \mathbf{E} + k^2 \mathbf{E} = 0, \nabla^2 \mathbf{H} + k^2 \mathbf{H} = 0, \quad (4)$$

where the propagation constant is defined as $k = k_0 n$, with n being the complex refractive index at incident wavelength λ . The solution of the above vector wave equation can be built from the separable scalar wave equation $\nabla^2 \psi + k^2 \psi = 0$ in spheroidal coordinate systems. Considering the spheroid is defined by the coordinates of a prolate, with the use of Laplacian ∇^2 in curvilinear coordinates, the resulting scalar wave equation can be written as³⁶.

$$\left[\frac{\partial}{\partial \eta} (1 - \eta^2) \frac{\partial}{\partial \eta} + \frac{\partial}{\partial \xi} (\xi^2 - 1) \frac{\partial}{\partial \xi} + \frac{\xi^2 - \eta^2}{(\xi^2 - 1)(1 - \eta^2)} \frac{\partial}{\partial \phi^2} \right] \psi + c^2 (\xi^2 - \eta^2) \psi = 0. \quad (5)$$

and implementing the separable of variables techniques, i.e., $\psi_{mn}(c; \eta) = S_{mn}(c; \eta) R_{mn}(c; \xi) \Phi(\phi)$, the above equation can be split into three separate ordinary differential equations.

$$\frac{d}{d\eta} \left[(1-\eta^2) \frac{d}{d\eta} S_{mn}(c;\eta) \right] + \left[\lambda_{mn} - c^2 \eta^2 - \frac{m^2}{1-\eta^2} \right] S_{mn}(c;\eta) = 0, \quad (6)$$

$$\frac{d}{d\xi} \left[(1-\xi^2) \frac{d}{d\xi} R_{mn}(c;\xi) \right] - \left[\lambda_{mn} - c^2 \eta^2 + \frac{m^2}{\xi^2-1} \right] R_{mn}(c;\xi) = 0, \quad (7)$$

where the solutions of $\Phi(\phi)$ are the sin and cosine functions. The angular $S_{mn}(c;\eta)$ and radial $R_{mn}(c;\xi)$ functions, respectively satisfy the above equations. The solution to this equation can be reconstructed from the three separate second order differential equations in η, ξ and ϕ , respectively, as follow.

$$\psi_{\epsilon_{mn}}^{(j)}(c;\eta,\xi,\phi) = S_{mn}(c;\eta) R_{mn}^{(j)}(c;\xi)_{\sin}^{\cos} m\phi, \quad (8)$$

Where j represents the kind of the radial function. For an arbitrary unit vector \mathbf{a} , the solution for the vector wave equation can be constructed from $\psi_{\epsilon_{mn}}^{(j)}(c;\eta,\xi,\phi)$, i.e., the spheroidal vector wavefunctions.

$$\begin{aligned} \mathbf{M}_{\epsilon_{mn}}^r &= \nabla \times (\mathbf{a} \psi_{\epsilon_{mn}}^{(j)}(c;\eta,\xi,\phi)), \\ \mathbf{N}_{\epsilon_{mn}}^r &= (1/k) \nabla \times \mathbf{M}_{\epsilon_{mn}}^r, \end{aligned} \quad (9)$$

in terms of which the fields inside and outside the particle can be expanded by using the appropriate kind of the radial function. By using the boundary conditions²⁷, the unknown coefficients in Eq. (2) and Eq. (3) can be obtained. All the corresponding quantities can be obtained, once the electric and magnetic fields are found.

Numerical Simulations.

To validate the results of the theory and experiment, scattering simulations under electromagnetic wave frequency domain using finite element solver COMSOL Multiphysics[®] were performed. The particle was surrounded by sufficient thick layer of air containing perfect mesh layer and scattering boundary conditions were used. The refractive index for the particle was taken as that of silicon at the optical wavelengths and for verification of experimental results the refractive index was calculated from the permittivity of ceramic $\epsilon' = 15.2$ while considering the tangent loss $\tan(\delta) \approx 10^{-4}$. The dimensions of the particle was taken the same as mentioned in the main text.

Sample fabrication. The sample was made of ceramics, the basis of the chemical composition of which is Mg-Ti-O. Measurement showed that the permittivity of ceramics at frequency of 6 GHz is $\epsilon' = 15.2$, $\tan(\delta) \approx 10^{-4}$. Such ceramics are well amenable to mechanical action, so it can be given any complex shape, including a spheroid with specific geometric parameters. In our work, we used a rectangular ceramic parallelepiped (1 cm \times 1 cm \times 5.5 cm), and after mechanical processing a superscattering particle with semi-major axis $a = 25.995$ mm and semi-minor axis $b = 4.985$ mm was obtained.

Experimental measurements. For the experimental observation of the PSHS, we used two helix antennas, LCP and RCP. The antennas were handcrafted and tested to meet the required specifications. The antenna and the sample were fixed on a rotating table, which allows maintaining the coaxiality of the wave vector \mathbf{k} of the incident field and the superscattering particle (see supplementary materials). The scattered field was detected by a rectangular waveguide, which measures only one component of the field at a time, along its short side. The antenna and waveguide were connected to a Rohde & Schwarz ZVB 20 vector analyzer. To extract the signal from a particle only, the S parameters of the system must be measured twice, with and without the particle, and then subtracted. The scattered intensity is a combination of two orthogonal components. Thus, to scan the full scattered field intensity for one polarization of the incident field, four measurements are required. To reduce noise, the measurements were averaged over 20 times.

Data availability

All data needed to evaluate the conclusions in this study is presented in the manuscript and in the Supplementary Information. The refractive index data can be taken as that of silicon in the desired frequency range.

References

1. Ling X, Zhou X, Huang K, Liu Y, Qiu C-W, Luo H, *et al.* Recent advances in the spin Hall effect of light. *Rep. Prog. Phys.* **80**, 066401 (2017)
2. Peng L, Ren H, Liu YC, Lan TW, Xu KW, Ye DX, *et al.* Spin Hall effect of transversely spinning light. *Sci. Adv.* **8**, eabo6033 (2022)
3. Yin X, Ye Z, Rho J, Wang Y, Zhang X. Photonic spin Hall effect at metasurfaces. *Science* **339**, 1405 (2013)
4. Hentschel M, Koshelev K, Sterl F, Both S, Karst J, Shamsafar L, *et al.* Dielectric Mie voids: confining light in air. *Light Sci. Appl.* **12**, 3 (2023)
5. Kivshar Y. The Rise of Mie-tronics. *Nano Lett.* **22**, 3513 (2022)
6. Hamidi M, Koshelev K, Gladyshev S, Valero AC, Hentschel M, Giessen H, *et al.* Quasi-Babinet principle in dielectric resonators and Mie voids. *Phys. Rev. Research* **7**, 013136 (2025)
7. Darwin CG. Notes on the theory of radiation. *Proc. R. Soc. Lond. A* **136**, 36 (1997)
8. Hosten O, Kwiat P. Observation of the spin Hall effect of light via weak measurements. *Science* **319**, 787 (2008)
9. Zhou X, Xiao Z, Luo H, Wen S. Experimental observation of the spin Hall effect of light on a nanometal film via

weak measurements. *Phys. Rev. A* **85**, 043809 (2012)

10. Bliokh KY, Niv A, Kleiner V, Hasman E. Geometrodynamics of spinning light. *Nat. Photon.* **2**, 748 (2008)
11. Nori F. The dynamics of spinning light. *Nat. Photon.* **2**, 716 (2008)
12. Kim M, Lee D, Yang Y, Kim Y, Rho J. Reaching the highest efficiency of spin Hall effect of light in the near-infrared using all-dielectric metasurfaces. *Nat. Commun.* **13**, 41467 (2022)
13. Kim M, Lee D, Nguyen TH-Y, Lee H-J, Byun G, Rho J. Total reflection-induced efficiency enhancement of the spin Hall effect of light. *ACS Photon.* **8**, 2705 (2021)
14. Li Z, Liu W, Cheng H, Chen S, Tian J. Manipulation of the photonic spin Hall effect with high efficiency in gold-nanorod-based metasurfaces. *Adv. Opt. Mater.* **5**, 1700413 (2017)
15. Luo W, Xiao S, He Q, Sun S, Zhou L. Photonic spin Hall effect with nearly 100% efficiency. *Adv. Opt. Mater.* **3**, 1102 (2015)
16. Gao D, Shi R, Miroshnichenko AE, Gao L. Enhanced Spin Hall Effect of Light in Spheres with Dual Symmetry. *Laser Photon. Rev.* **12**, 1800130 (2018)
17. Olmos-Trigo J, Sanz-Fernández C, García-Etxarri A, Molina-Terriza G, Bergeret FS, Sáenz JJ. Enhanced spin-orbit optical mirages from dual nanospheres. *Phys. Rev. A* **99**, 013852 (2019)
18. Zambrana-Puyalto X, Fernandez-Corbaton I, Juan ML, Vidal X, Molina-Terriza G. Duality symmetry and Kerker conditions. *Opt. Lett.* **38**, 1857 (2013)
19. Sun Y, Xu P, Gao L, Miroshnichenko AE, Gao D. Wavelength-scale spin Hall shift of light with morphology-enhanced scattering efficiency from nanoparticles. *Laser Photon. Rev.* **16**, 202200289 (2022)
20. Ruan Z, Fan S. Superscattering of light from subwavelength nanostructures. *Phys. Rev. Lett.* **105**, 013901 (2010)
21. Canos Valero A, Shamkhi HK, Kupriianov AS, Weiss T, Pavlov AA, Redka D, *et al.* Superscattering emerging from the physics of bound states in the continuum. *Nat. Commun.* **14**, 4689 (2023)
22. Kuznetsov AV, Canos Valero A, Shamkhi HK, Terekhov P, Ni X, Bobrovs V, *et al.* Special scattering regimes for conical all-dielectric nanoparticles. *Sci. Rep.* **12**, 21904 (2022)
23. Haefner D, Sukhov S, Dogariu A. Spin hall effect of light in spherical geometry. *Phys. Rev. Lett.* **102**, 123903 (2009)
24. Soni J, Mansha S, Dutta Gupta S, Banerjee A, Ghosh N. Giant Goos-Hänchen shift in scattering: the role of interfering localized plasmon modes. *Opt. Lett.* **39**, 4100 (2014)
25. Olmos-Trigo J, Sanz-Fernández C, Abujetas DR, Lasa-Alonso J, de Sousa N, García-Etxarri A, *et al.* Kerker conditions upon lossless, absorption, and optical gain regimes. *Phys. Rev. Lett.* **125**, 073205 (2020)
26. Qian C, Lin X, Yang Y, Xiong X, Wang H, Li E, *et al.* Experimental observation of superscattering. *Phys. Rev. Lett.* **122**, 063901 (2019)
27. Asano S, Yamamoto G. Light scattering by a spheroidal particle. *Appl. Opt.* **14**, 29 (1975)
28. Rybin MV, Koshelev KL, Sadrieva ZF, Samusev KB, Bogdanov AA, Limonov MF, *et al.* High-Q supercavity modes in subwavelength dielectric resonators. *Phys. Rev. Lett.* **119**, 243901 (2017)
29. Arnoldus HF, Li X, Shu J. Subwavelength displacement of the far-field image of a radiating dipole. *Opt. Lett.* **33**, 1446 (2008)

30. Kim M, Yang Y, Lee D, Kim Y, Kim H, Rho J. Spin Hall effect of light: from fundamentals to recent advancements. *Laser Photon. Rev.* **17**, 2200046 (2022)
31. Bliokh KY, Ostrovskaya EA, Alonso MA, Rodriguez-Herrera OG, Lara D, Dainty C. Spin-to-orbital angular momentum conversion in focusing, scattering, and imaging systems. *Opt. Express* **19**, 26132 (2011)
32. Bliokh KY, Rodríguez-Fortuño FJ, Nori F, Zayats AV. Spin-orbit interactions of light. *Nat. Photon.* **9**, 796 (2015)
33. Pan D, Wei H, Gao L, Xu H. Strong spin-orbit interaction of light in plasmonic nanostructures and nanocircuits. *Phys. Rev. Lett.* **117**, 166803 (2016)
34. Rodríguez-Herrera OG, Lara D, Bliokh KY, Ostrovskaya EA, Dainty C. Optical nanoprobng via spin-orbit interaction of light. *Phys. Rev. Lett.* **104**, 253601 (2010)
35. Li X, Shu J, Arnoldus HF. Far-field detection of the dipole vortex. *Opt. Lett.* **33**, 2269 (2008)
36. Li L-W, Kang X-K, Leong M-S. *Spheroidal wave functions in electromagnetic theory*. John Wiley & Sons, 2004.

Acknowledgements

This work was supported by National Natural Science Foundation of China (12174281, 12274314, 12311530763); Natural Science Foundation of Jiangsu Province (BK20221240); Suzhou Basic Research Project (SJC2023003). The calculations of non-Hermitian superscattering are partially supported by Russian Science Foundation (23-72-00037).

Author Contributions

These authors contributed equally: Aizaz Khan, Nikolay Solodovchenko.

Competing interests

The authors declare no competing interests.

Supplementary Information for

“Direct observation of photonic spin Hall effect in Mie scattering”

Aizaz Khan^{1,2,†}, Nikolay Solodovchenko^{3,†}, Dongliang Gao^{1*}, Denis Kislov⁴, Xiaoying Gu¹, Yuchen Sun⁵, Lei Gao^{1,2*}, Cheng-Wei Qiu^{6*}, Alexey Arsenin⁴, Alexey Bolshakov⁴, Vjaceslavs Bobrovs⁷, Alexander S. Shalin^{2,4,8,9*}

¹ School of Physical Science and Technology, Soochow University, Suzhou 215006, China & Jiangsu Key Laboratory of Frontier Material Physics and Devices, Soochow University, Suzhou 215006, China.

² School of Optical and Electronic Information, Suzhou City University & Suzhou Key Laboratory of Biophotonics & Jiangsu Key Laboratory of Biophotonics, Suzhou 215104, China.

³ School of Physics and Engineering, ITMO University, Saint-Petersburg 197101, Russia.

⁴ Moscow Center for Advanced Studies, Kulakova str. 20, Moscow 123592, Russia.

⁵ School of Electrical and Electronic Engineering, 50 Nanyang Avenue, Nanyang Technological University, Singapore, 639798, Singapore.

⁶ Department of Electrical and Computer Engineering, National University of Singapore, Singapore 117583, Singapore.

⁷ Riga Technical University, Institute of Photonics, Electronics and Telecommunications, 1048 Riga, Latvia

⁸ Centre for Photonic Science and Engineering, Skolkovo Institute of Science and Technology, Moscow, 121125, Russia.

⁹ Beijing Institute of Technology Beijing 100081, China

Table of Contents:

- S1.** Relation of spin Hall shift and scattering intensity with the Poynting vector
- S2.** Derivation of explicit relation between PSHS and scattering intensity for spheroidal particle
- S3.** Relation of spin Hall shift and scattering intensity with the scattering coefficients
- S4.** The scattering cross-section
- S5.** Demonstration of near-field spin-orbit interaction
- S6.** Simulation methods

S1. Relation of spin Hall shift and scattering intensity with the Poynting vector:

The photonic spin Hall shift (PSHS) in scattering is commonly associated with the two eigenmodes: left circular polarized (LCP) and right circular polarized light (RCP), which can be treated as pure states of polarization with defined helicity¹. In a spherical coordinates system, the angular S_θ and azimuthal S_ϕ components of the Poynting vector are associated with transversal energy flow and are directly responsible for the apparent displacement of the position of the scatterer in both the longitudinal and the transverse directions, respectively. However, the angular component, which is independent of polarization, primarily governs the shift in the longitudinal direction and is the analog of Goos-Hänchen shift at the scale of scattering

from a single particle. On the other hand, the shift in the position of the particle due to spin-orbit interaction (SOI), as perceived in the far-field, is determined by the azimuthal component, which can be calculated using Mie theory^{1, 2, 3}.

$$\Delta_{\text{SH}} = \lim_{r \rightarrow \infty} r(-S_{\phi} / S_r) \hat{\phi}, \quad (\text{S1})$$

where, S_r represent the radial component of the scattered Poynting vector \mathbf{S} . The definition for the far-field PSHS holds true for a spherical, cylindrical or spheroidal scatterer, provided that a suitable transformation from spheroidal coordinates has been implemented. To enhance scattering via mode coupling, spherical symmetry should be broken. In such cases, the PSHS for spheroidal scatterers can be obtained by using the above definition under far-field approximation. The corresponding far-field scattered intensity in the far-field limit can be found by using the relation.

$$i(\theta) = (kr)^2 (E_{\xi} E_{\xi}^* + E_{\eta} E_{\eta}^*). \quad (\text{S2})$$

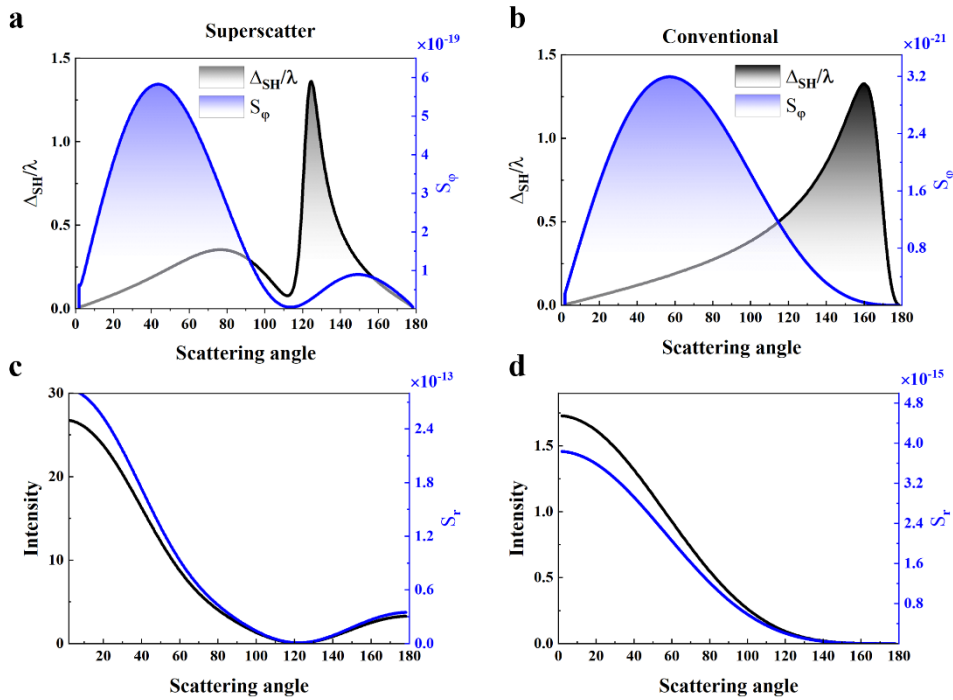


Fig. S1| Dependence of PSHS and scattering intensity on azimuthal and radial components of Poynting vector: PSHS and the azimuthal component of the Poynting vector for **a** superscatterer **b** conventional spherical scatterer with diameter 219 nm. The azimuthal component at the maximal PSHS is enhanced rather than sufficiently suppressed radial component for the superscatterer. The far-field scattered intensity follows the same trend as the radial component of the Poynting vector. Scattered intensity and the radial component of Poynting vector along the scattering angle for **c** superscatterer and **d** conventional scatterer. The superscattering particle is a prolate spheroid with semi-major axis $a=500$ nm and semi-minor axis $b=100$ nm. The incident wavelength is 890 nm.

Although, the radial component of the scattered electric field vanishes in the far-field, the scattering

intensity exhibits the same variations as S_r , as shown in Fig. S1a. According to the definition of PSHS, enhancing PSHS in higher dimensions requires an increase in the ratio of the azimuthal to the radial component. While the azimuthal component typically has a small magnitude, a depth in the S_r at certain scattering angle can boost the PSHS, leading to lower scattering intensity at the maximal PSHS. This is what commonly observed at the extreme backscattered direction in scattering from conventional scatterers, as shown in Fig. S1. In stark contrast to this, due to enhance scattering and helical flow both the radial and azimuthal components of the Poynting vector are boosted by at the angle of maximal PSHS, as shown in Fig. S1. Thus, by maximizing the light-matter interaction through superscattering, one can obtain enhance scattering intensity with preserved PSHS, provided that strong spin-orbit interaction appears in the near-field together with overlapping multipoles in phase, as we shall discuss in the following sections.

S2. Derivation of explicit relation between PSHS and scattering intensity for spheroidal particle:

Without the loss of generality, we assume a spheroidal superscatterer, which is governed by its semi-major axis a , semi-minor axis b and focal length d and is illuminated by LCP light propagating along the z -axis, i.e., $E^{inc} = e^{ikz}(\hat{x} - i\hat{y})$. For brevity, the propagating direction is taken parallel to the semi-major axis a of the spheroidal superscatterer. The size parameter q is defined as $q = ka$, where k is the free-space wavevector. By employing the components of scattered electric and magnetic fields, one can obtain the corresponding components of the Poynting vector. The incident electric and magnetic fields can be expressed in terms of spheroidal vector wave functions $N_{emn}^{(i)}$ and $M_{emn}^{(i)}$ ⁴,

$$\mathbf{E}^{inc} = \sum_{n=1}^{\infty} i^n (g_n \mathbf{M}_{omn}^{(1)} - if_n \mathbf{N}_{emn}^{(1)} + ig_n \mathbf{M}_{emn}^{(1)} - f_n \mathbf{N}_{omn}^{(1)}), \mathbf{H}^{inc} = \frac{k}{i\omega\mu} \sum_{n=1}^{\infty} i^n (g_n \mathbf{N}_{omn}^{(1)} - if_n \mathbf{M}_{emn}^{(1)} + ig_n \mathbf{N}_{emn}^{(1)} - f_n \mathbf{M}_{omn}^{(1)}). \quad (S3)$$

where, the coefficients of the incident field are related, $g_n = f_n$ and can be defined as,

$$g_n = \frac{2}{\sum_{r=0,1}^{\infty} \frac{2(r+2)!}{(2r+3)r!} (d_r^{mn})^2} \sum_{r=0,1}^{\infty} 'd_r^{mn}, \quad (S4)$$

where d_r^{mn} is the expansion coefficient related to the spheroidal coordinates systems whereas the prime in the summation shows that the summation is only over even values, if the difference $n - m$ is even, otherwise, it is only over odd⁴. Under normal incidence, m can be taken as unity. To derive the PSHS, one needs the scattered

electric and magnetic fields which can be expressed in terms of the spheroidal vector wave functions.

$$\mathbf{E}^{sca} = \sum_{n=1}^{\infty} i^n \left(i\alpha_n \mathbf{N}_{emn}^{(3)} - \beta_n \mathbf{M}_{emn}^{(3)} + \alpha_n \mathbf{N}_{emn}^{(3)} - i\beta_n \mathbf{M}_{emn}^{(3)} \right), \mathbf{H}^{sca} = \frac{k}{i\omega\mu} \sum_{n=1}^{\infty} i^n \left(i\alpha_n \mathbf{M}_{emn}^{(3)} - \beta_n \mathbf{N}_{emn}^{(3)} + \alpha_n \mathbf{M}_{emn}^{(3)} - i\beta_n \mathbf{N}_{emn}^{(3)} \right), \quad (\text{S5})$$

Similarly, the internal fields are given by,

$$\mathbf{E}^{in} = \sum_{n=1}^{\infty} i^n \left(\delta_n \mathbf{M}_{emn}^{(1)} - i\gamma_n \mathbf{N}_{emn}^{(1)} + i\delta_n \mathbf{M}_{emn}^{(1)} - \gamma_n \mathbf{N}_{emn}^{(1)} \right), \mathbf{H}^{in} = \frac{k}{i\omega\mu} \sum_{n=1}^{\infty} i^n \left(\delta_n \mathbf{N}_{emn}^{(1)} - i\gamma_n \mathbf{M}_{emn}^{(1)} + i\delta_n \mathbf{N}_{emn}^{(1)} - \gamma_n \mathbf{M}_{emn}^{(1)} \right), \quad (\text{S6})$$

where, $\alpha_n, \beta_n, \delta_n$ and γ_n represents the unknown coefficients corresponding to scattered and internal fields, which are to be determined by numerically solving the boundary conditions at the interface⁴, whereas the spheroidal vector wave functions $\mathbf{M}_{emn}^{(j)}$ and $\mathbf{N}_{emn}^{(j)}$ can be obtained by solving the Helmholtz equation in spheroidal coordinates using separation of variables³. Under far-field approximation, the asymptotic forms of the third kind of spheroidal vector wave functions are given as.

$$M_{\epsilon_{mn},\xi}^{(3)} = \mp(-i)^{n+1} m \cos \theta \left(\frac{d}{2} \right)^2 S_{mn}(\cos \theta) \left(\frac{1}{kr^3} \right) e^{ikr} \times_{-\cos}^{\sin} m\phi, \quad (\text{S7})$$

$$M_{\epsilon_{mn},\eta}^{(3)} = (-i)^{n+1} m \frac{S_{mn}(\cos \theta)}{\sin \theta} \frac{1}{kr} e^{ikr} \times_{-\cos}^{\sin} m\phi, \quad (\text{S8})$$

$$M_{\epsilon_{mn},\phi}^{(3)} = -(-i)^{n+1} \frac{dS_{mn}(\cos \theta)}{d\theta} \frac{1}{kr} e^{ikr} \times_{\sin}^{\cos} m\phi, \quad (\text{S9})$$

Similarly,

$$N_{\epsilon_{mn},\xi}^{(3)} = (-i)^{n+1} \left(\frac{m^2 S_{mn}(\cos \theta)}{\sin^2 \theta} - \cot \theta \frac{dS_{mn}(\cos \theta)}{d\theta} - \frac{d^2 S_{mn}(\cos \theta)}{d\theta^2} \right) \left(\frac{1}{kr} \right)^2 e^{ikr} \times_{\sin}^{\cos} m\phi, \quad (\text{S10})$$

$$N_{\epsilon_{mn},\eta}^{(3)} = -(-i)^n \left(\frac{dS_{mn}(\cos \theta)}{d\theta} \right) \left(\frac{1}{kr} \right) e^{ikr} \times_{\sin}^{\cos} m\phi, \quad (\text{S11})$$

$$N_{\epsilon_{mn},\phi}^{(3)} = -(-i)^n m \left(\frac{S_{mn}(\cos \theta)}{\sin \theta} \right) \left(\frac{1}{kr} \right) e^{ikr} \times_{-\cos}^{\sin} m\phi. \quad (\text{S12})$$

Where the subscript ξ, η and ϕ corresponds to the spheroidal coordinates, whose unit vectors are correlated to the unit-vectors in spherical coordinates as, $\hat{\xi} \rightarrow \hat{r}$, $\hat{\eta} \rightarrow -\hat{\theta}$ and $\hat{\phi} \rightarrow \hat{\phi}$. Using the above spheroidal vector wave functions and the scattered field coefficients obtained from the boundary conditions, the scattered field and, hence, the Poynting vector \mathbf{S} corresponding to the scattered field can be computed. Using equation S1, the far-field PSHS can be obtained, which is given in explicit form as follows³.

$$\Lambda_{SH}(\theta) = \frac{1}{k} \times \text{Re} \left[\frac{1}{i(\theta)} \left(\sum_{n=1}^{\infty} \alpha_n \left(\frac{\sigma_n}{\sin(\theta)} - \frac{1}{\tan(\theta)} \chi_n - \frac{d\chi_n}{d\theta} \right) \times \sum_{n=1}^{\infty} (\sigma_n \alpha_n + \chi_n \beta_n)^* + \sum_{n=1}^{\infty} \left(\beta_n \left(\frac{\sigma_n}{\sin(\theta)} - \frac{1}{\tan(\theta)} \chi_n - \frac{d\chi_n}{d\theta} \right) \right)^* \times \sum_{n=1}^{\infty} (\chi_n \alpha_n + \sigma_n \beta_n) \right) \right].$$

(S13)

Here, σ_n and χ_n are the angular functions which are given as $S_{1n} \cos(\theta) / \sin(\theta)$ and $d(S_{1n} \cos(\theta)) / d\theta$, respectively, whereas $i(\theta)$ as demonstrated by Eq. (S2) is the far-field scattering intensity given as,

$$i(\theta) = \left| \sum_{n=1}^{\infty} (\alpha_n \chi_n(\theta) + \beta_n \sigma_n(\theta)) \right|^2 + \left| \sum_{n=1}^{\infty} (\alpha_n \sigma_n(\theta) + \beta_n \chi_n(\theta)) \right|^2, \quad (\text{S14})$$

The scattering intensity naturally arises in the definition of the PSHS irrespective of the scatterer's morphology. It is crystal clear from the above relation that the resulting PSHS is inversely related to the far-field scattered intensity. This behavior can be observed for both conventional and superscattering particles from Fig. S1. This is the fate of PSHS at the scale of a single particle, where the simultaneous enhancement of the scattered field intensity and PSHS cannot be realized even under normal incidence, as demonstrated in the earlier section. That is, the enhanced PSHS at a certain scattering angle is naturally tied to vanishingly small far-field scattering intensity and vice versa. It is important to note that the PSHS is not only the function of scattered angle but also depends upon the optical properties of the scatterer². The above equation reduces to that of the spherical particle, when the aspect ratio is 1, while ignoring the fast-decaying terms d_r^{11} in the dipolar approximation (considering only the electric and magnetic dipoles).

S3. Relation of spin Hall shift and scattering intensity with the scattering coefficients:

The interference between the multipoles exhibits important role in enhancing PSHS^{5, 6}. Due to mode coupling, the contribution to scattering from one or several multipoles can be boosted. Therefore, the amplitude of the PSHS in the perceived location can be altered by the number of multipole terms in the expansion of scattered field, especially when the contributions from several multipoles to scattering is enhanced. From equation S13, it is obvious that the far-field intensity is in proportion with the amplitude of the coefficients of the scattered field. The simultaneous enhancement of the PSHS and the intensity requires the scattered coefficients to overlap at their resonances rather than at their tails³. Such a scenario is realized in conventional quasi-dual scatterer when the condition $\alpha_1 \approx \beta_1$ is satisfied, which enforces high forward directional scattering in the forward direction, i.e., when the dipolar modes constructively interfere in the forward direction. The destructive interference in the backscattered direction leads to enhance the PSHS at the tail of the scattering angle.

S4. The scattering cross-section:

The scattering cross-section of a scatterer immersed in a non-absorbing host medium is defined as $\sigma_{\text{sca}} = \lim_{r \rightarrow \infty} 4\pi r^2 |\mathbf{E}_s|^2 / |\mathbf{E}_i|^2$, where r is the radial distance, \mathbf{E}_s is the scattered electric field and \mathbf{E}_i is the incident electric field. By using the expansion of scattered and incident fields in the spheroidal vector wave functions, one obtained the following relation of the scattered field⁴.

$$\sigma_{\text{sca}} = \frac{\lambda^2}{4\pi} \sum_{n=1}^{\infty} \left(\Pi_{nn}^m \text{Re}(|\alpha_{nn'}|^2 + |\beta_{nn'}|^2) \right). \quad (\text{S15})$$

$$\sigma_{\text{sca}} = \frac{\lambda^2}{\pi} \left[\sum_{n=1}^{\infty} \left[\beta_n \frac{S_{1n}(\cos \theta)}{\sin \theta} + \alpha_n \frac{d[S_{1n}(\cos \theta)]}{d\theta} \right]^2 \sin^2 \phi + \sum_{n=1}^{\infty} \left[\beta_n \frac{d[S_{1n}(\cos \theta)]}{d\theta} + \alpha_n \frac{S_{1n}(\cos \theta)}{\sin \theta} \right]^2 \cos^2 \phi \right]. \quad (\text{S16})$$

The total cross-section of the spheroidal obtained so far is not a simple equation, due to the presence of the function Π_{nn}^m , however, it is well-known that for spherical symmetric scatterer, the total contribution from a single channel cannot exceed the single channel limit, that is the maximum cross-section according to the current established limit is defined as, $\sigma_{\text{sca}}^{\text{max}} = (2n+1)\lambda^2 / 2\pi$. With n being the expansion coefficient. We normalized the scattering cross-section of each channel by the single channel limit as given in the main text.

S5. Demonstration of Spin Orbit interaction in the Near-Field:

Spin and orbital angular momentum are the fundamental dynamical properties associated with optical fields that aligns with the propagation direction and remains uncoupled in free-space. During scattering, stark contrast of optical constants at the interface of air and a high-index non-magnetic dielectric particle, sharp potential gradient arises which mediates strong coupling of the polarization and spatial degree of freedom. Spin-orbit interaction in the near-field is considered as the origin of PSHS. To characterize this near-field spin-orbit interaction, Maxwell's equations can be reformulated in a Dirac-like framework using optical potential V and Dirac matrices $\hat{\alpha}_i$ ($i=1,2,3$) and $\hat{\beta}$. The concise Dirac-like equation is given as below^{7, 8, 9}.

$$c(\hat{\alpha} \cdot \hat{p})\Psi + \hat{\beta}V\Psi = i\partial\Psi / \partial t, \quad (\text{S17})$$

where $\Psi = (4\omega)^{-1/2} (\epsilon_0^{1/2} \mathbf{E}, \mu_0^{1/2} \mathbf{H})^T$ denotes the wavefunction constructed by the electric and magnetic fields and \hat{p} is the canonical momentum operator, whose expectation value $\langle \Psi | \hat{p} | \Psi \rangle$ is directly related with the orbital

momentum density \mathbf{p}^o ⁸.

$$\mathbf{p}^o = (4\omega)^{-1} \text{Im}[\varepsilon_0 \mathbf{E}^* (\nabla) \mathbf{E} + \mu_0 \mathbf{H}^* (\nabla) \mathbf{H}]. \quad (\text{S18})$$

The orbital momentum density defines the trajectory of photons as optical currents, and provides a better intuition on how the photons do evolve therein. On the other hand, the local spin density is related with $\langle \Psi | \hat{\mathbf{a}} | \Psi \rangle$. Thus, the first term in equation S17 demonstrates the coupling of both spin and orbital angular momentum. Upon spin-orbit interaction in the near-field, the field loses its spin as a result of transformation to orbital angular momentum and consequently the field-near the scatterer changes its polarization which differs from that of the incident light and far-field. This is only true in the regions of strong spin-orbit interaction. Thus, polarization analysis of the field in the vicinity of the particle would directly probe the spin-orbit coupling. The circular polarization degree in terms of total field is given as follow⁷:

$$\text{CPD} = |\varepsilon_0 \mathbf{E}^* \times \mathbf{E} + \mu_0 \mathbf{H}^* \times \mathbf{H}| / (\varepsilon_0 |\mathbf{E}|^2 + \mu_0 |\mathbf{H}|^2). \quad (\text{S19})$$

S6. Simulations Methods:

All the results were confirmed by numerically solving Maxwell's equations using finite element solver, COMSOL Multiphysics. The particles were immersed in air and the refractive index that defines the optical properties of the particles were taken from the experimental data of silicon. The particle long axis of the particle was taken along the direction of propagating wave, and scattering boundary conditions were used. After computing the electric and magnetic fields, all the near-field and far-field quantities were calculated using their corresponding expressions.

References

1. Soni J, Mansha S, Dutta Gupta S, Banerjee A, Ghosh N. Giant Goos-Hänchen shift in scattering: the role of interfering localized plasmon modes. *Opt. Lett.* **39**, 4100 (2014)
2. Haefner D, Sukhov S, Dogariu A. Spin Hall effect of light in spherical geometry. *Phys. Rev. Lett.* **102**, 123903 (2009)
3. Sun Y, Xu P, Gao L, Miroshnichenko AE, Gao D. Wavelength-scale spin Hall shift of light with morphology-enhanced scattering efficiency from nanoparticles. *Laser Photon. Rev.* **16**, 202200289 (2022)
4. Asano S, Yamamoto G. Light-scattering by a spheroidal particle. *Appl. Opt.* **14**, 29 (1975)
5. Olmos-Trigo J, Sanz-Fernández C, Abujetas DR, García-Etxarri A, García-Martín A. Optical Mirages from Spinless Beams. *ACS Photon.* **10**, 1742 (2023)
6. Gao D, Shi R, Miroshnichenko AE, Gao L. Enhanced spin Hall effect of light in spheres with dual symmetry. *Laser Photon. Rev.* **12**, 1800130 (2018)

7. Pan D, Wei H, Gao L, Xu H. Strong Spin-Orbit Interaction of Light in Plasmonic Nanostructures and Nanocircuits. *Phys. Rev. Lett.* **117**, 166803 (2016)
8. Bliokh KY, Bekshaev AY, Nori F. Extraordinary momentum and spin in evanescent waves. *Nat. Commun.* **5**, 3300 (2014)
9. Mignani E, Recami E, Baldo M. About a dirac-like equation for the photon according to etto majorana. *Lett. al Nuovo Cimento (1971-1985)* **11**, 568 (1974)